FLARING ARCHES

I. *The Major Events of 1980 November 6 and 12*

SARA F. MARTIN

Solar Astronomy, CALTECH, Pasadena, CA 91125, U.S.A.

and

ZDENĚK F. ŠVESTKA

Laboratory for Space Research, SRON, The Netherlands

(Received 4 February; in revised form 5 April, 1988)

Abstract. 'Flaring arches' is a name assigned to a particular component of some flares. This component consists of X-ray and Hα emission which traverses a coronal arch from one to the other of its chromospheric footpoints. The primary footpoint is at the site of a flare. The secondary footpoint, tens of thousands of kilometers distant from the source flare, but in the same active region, brightens in Hα concurrent with the beginning of the hard X-ray burst at the primary site. From the inferred travel time of the initial exciting agent we deduce that high speed electron streams travelling through the arch must be the source of the initial excitation at the secondary footpoint. Subsequently, a more slowly moving agent gradually enhances the arch first in X-rays and subsequently in Hα, starting at the primary footpoint and propagating along the arch trajectory. The plasma flow in Hα shows clearly that material is injected into the arch from the site of the primary footpoint and later on, at least in some events, a part of it is also falling back.

Thus a typical flaring arch has three, and perhaps four consecutive phases: (1) An early phase characterized by the onset of hard X-ray burst and brightening of the secondary footpoint in Hα. (2) The main X-ray phase, during which X-ray emission propagates through the arch. (3) The main Hα phase, during which Hα emitting material propagates through the arch. And (4) an aftermath phase when some parts of the ejected material seem to flow in the reverse direction towards the primary site of injection.

An extensive series of flaring arches was observed from 6 to 13 November, 1980 at the Big Bear Solar Observatory and with the Hard X-Ray Imaging Spectrometer (HXIS) on board the SMM in a magnetically complex active region. The two most intense arches for which complete Hα and X-ray data are available and which occurred on 6 November at 17 : 21 UT (length ≈57 000 km) and on 12 November at 16 : 57 UT (length ≈263 000 km) are discussed in this paper.

1. Introduction

The Hα emitting mass that constitutes the lower-temperature parts of solar flares has several characteristic morphological forms. Common to the vast majority of flares are the chromospheric flare elements at the base of coronal flare loops. We identify these as the 'primary footpoints'. Many flares also exhibit peripheral or remote chromospheric brightenings (e.g., Rust and Webb, 1977; Martin, 1979; Tang, 1982; Duijveman, Hoyng, and Machado, 1982). The peripheral brightenings begin seconds to minutes after the primary footpoints either in another part of the active region or in the quiet chromosphere surrounding the active region. In this paper we refer to the remote brightenings as 'secondary footpoints'.

In addition to these chromospheric flare components, time-lapse series of Hα photographs have revealed at least five other forms of Hα emission which constitute coronal

Solar Physics **116** (1988) 91–118.

aspects of solar flares and flare-associated events. As summarized by Martin (1979), these are:

(1) growing systems of flare loops,

(2) emission traversing coronal arcs,

(3) brightened filament mass and/or erupting filament mass (sprays),

(4) bright surges,

(5) diffuse, faint, moving emissions described usually as flare waves or emission fronts.

The objective of this paper is to present a detailed description of the second category above. These flare-related phenomena have been seldom mentioned and illustrated in previous literature. Some examples that we have found in previous papers were identified (or misidentified) under a different name. An excellent series of three Hα pictures of a flaring arch is shown in Bruzek (1967), but this event was misidentified as an arch filament system. At least two flaring arches are included in the Rust, Simnett, and Smith (1985) study and list of fast-moving 'thermal wave fronts' identified in X-ray images. The descriptive phrase 'emission traversing coronal arcs' was introduced by Martin (1979) and was the first attempt to distinguish this type of event from other Hα emission components of flares. Following Martin and Švestka (1987), in this paper we will use the shorter name 'flaring arches' for these phenomena. This term has also been used by Mouradian, Martres, and Soru-Escaut (1983) for describing several forms of flare emission that is transported through the lower corona; the one illustrated in their Figure 6 might be the same phenomenon we describe in this paper.

Recently we have identified several series of flaring arches in high-resolution Hα data from the Big Bear Solar Observatory and in images in 3.5–30 keV X-rays from the Hard X-Ray Imaging Spectrometer (HXIS; Van Beek *et al.*, 1980) flown on the Solar Maximum Mission spacecraft. In this paper we concentrate our attention to only two major events, observed on 6 and 12 November, respectively. They were the brightest events of this kind found to date during the first interval of SMM operations (in 1980). Both were well observed in the Hα line and in X-rays, and are representative examples of this class of phenomena. In Paper II we will discuss this kind of activity in a broader content, considering observations of several more events of flaring arches in this active region and discussing their relationship to other forms of flare-associated emission.

2. The Data

The flaring arches discussed in this and the following paper (Švestka *et al.*, 1988, Paper II) were observed in the active region No. 2779 (Hale No. 17255, latitude S11, CMP date 11 November, 1980, cf. *Solar Geophysical Data*, 1981a). The Big Bear Solar Observatory observed this active region in the interval 6–13 November, and HXIS from 6–12 November, 1980.

The two brightest flaring arches were observed at 17 : 21 UT on 6 November and at 16 : 57 UT on 12 November, 1980. Though both occurred in the same active region, they appeared in different arch systems. The 6 November event (Figure 1) was very bright

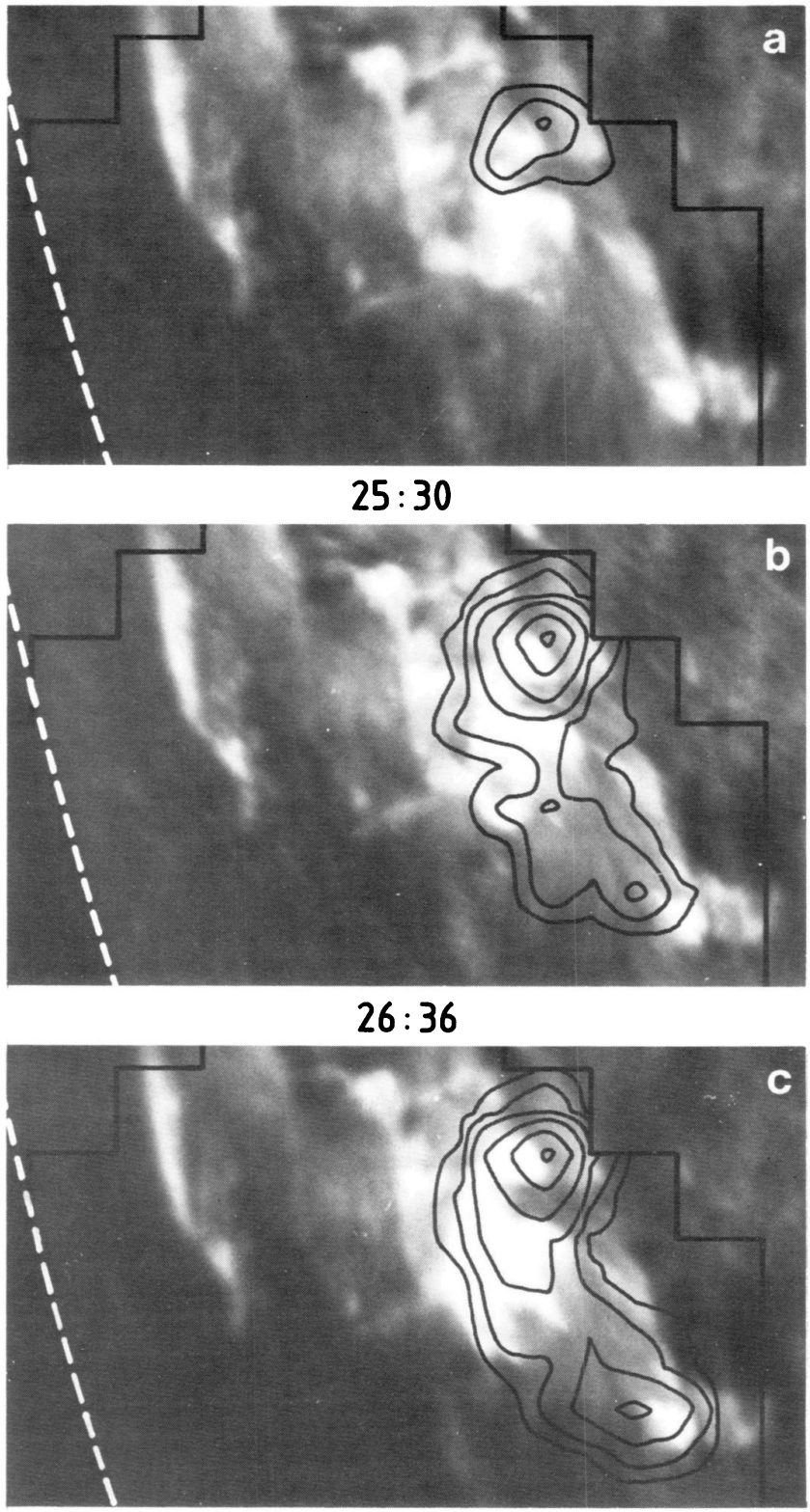

Fig. 1a–c. Growth of the X-ray arch: (a) $t(\mathrm{H}\alpha) = 17:24:57$ UT, $t(\mathrm{X}) = 17:25:30$ UT, $F_M = 17$ counts; (b) $t(\mathrm{H}\alpha) = 17:25:57$ UT, $t(\mathrm{X}) = 17:26:36$ UT, $F_M = 152$ counts; (c) $t(\mathrm{H}\alpha) = 17:27:22$ UT, $t(\mathrm{X}) = 17:27:41$ UT, $F_M = 134$ counts.

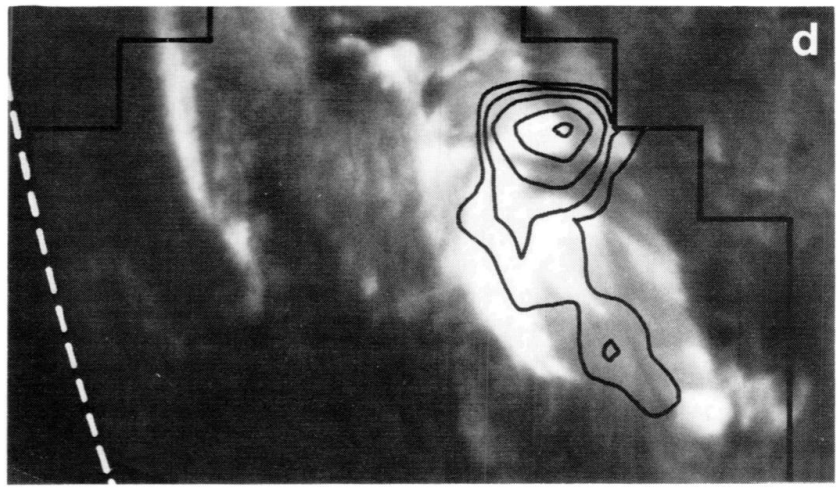

28:46

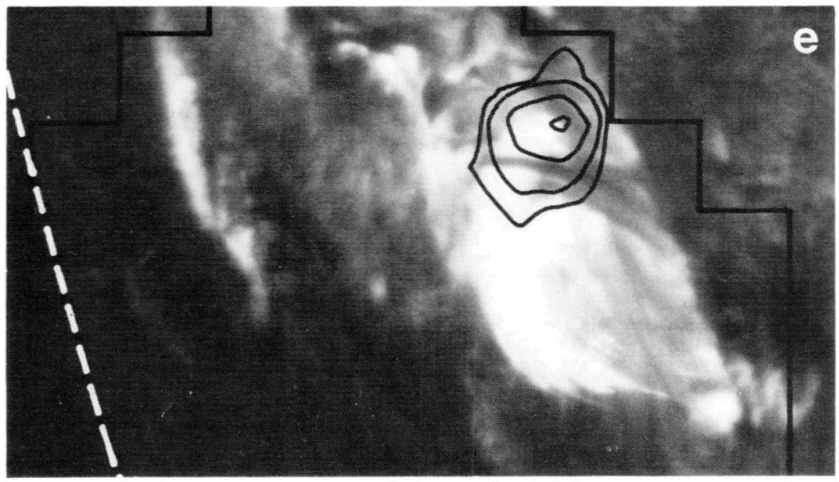

29:47

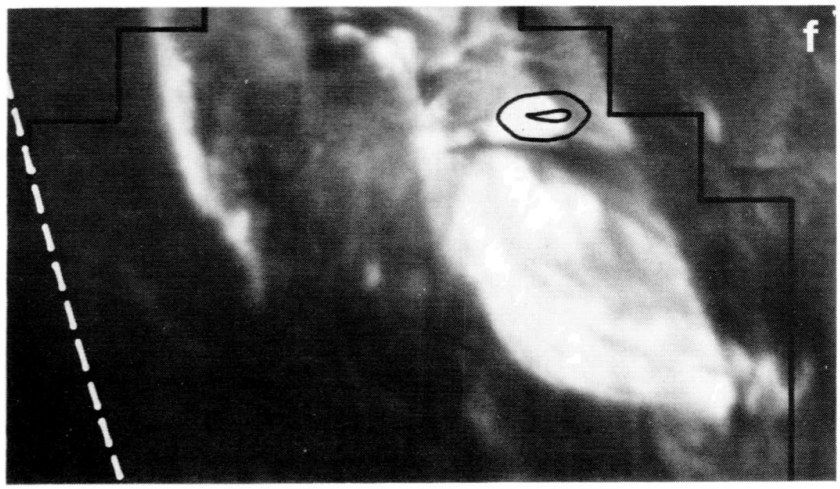

32:03

Fig. 1d–f. Decay of the X-ray arch: (d) $t(\mathrm{H}\alpha) = 17:28:12$ UT, $t(\mathrm{X}) = 17:28:46$ UT, $F_M = 90$ counts; (e) $t(\mathrm{H}\alpha) = 17:29:44$ UT, $t(\mathrm{X}) = 17:29:47$ UT, $F_M = 41$ counts; (f) $t(\mathrm{H}\alpha) = 17:31:59$ UT, $t(\mathrm{X}) = 17:32:03$ UT, $F_M = 9$ counts.

in Hα and was associated with an intense hard X-ray burst, but it was relatively small; the distance between the arch footpoints was 37 000 km and the real length of the arch was estimated to be 57 000 km. The 12 November event (Figure 2) was less bright in Hα and the associated hard X-ray flux (>30 keV) was only about one half of that on 6 November, but the arch was much larger: the distance between the footpoints was 150 000 km and the estimated real length of the arch system was 263 000 km. In spite of these differences in size and location, both flaring arches had many basic properties in common. In order to simplify the following discussion, we will talk about the SB (small and bright) arch on 6 November and the L (large) arch on November 12.

3. Common Characteristics

3.1. Flow of Hα-emitting material

In Hα images one can see material at chromospheric temperatures flowing from the primary to the secondary footpoint through a pre-existing arch system; the flaring arch consists of many fine, nearly parallel threads of emission, as one can see particularly well in Figure 1(e) and the flow speed seems to be slightly different in different threads. The average speed of this flow was 114 km s^{-1} in the SB arch and 260 km s^{-1} in the L arch. The time developments of the flow speed, however, were different in the two arches, as Table I clearly demonstrates.

In the SB arch, the flow speed was high at the onset of the event and decelerated with time: from >290 km s^{-1} at 17 : 26 UT to ~26 km s^{-1} at 17 : 33 UT. In the L arch, on the other hand, the speed was slightly increasing in the initial phase prior to 17 : 03 UT, and stayed more or less constant thereafter; lower speeds are measured after 17 : 07 UT, but these values most probably belong to another component of the injection which prevails in the Hα images after that time. In this case the faster Hα flow had a mean speed of 392 km s^{-1} and the slower one 239 km s^{-1}.

When extrapolated backwards under the assumption that these speeds in the L arch were constant, the slower ejection would have originated at 16 : 59 UT and the faster one close to 17 : 01 UT. These onset times are somewhat uncertain, first because of the assumption of constant speed, and second because the Hα might not show the real motion of the cooled material: if the ejected material was at coronal temperature, then

Fig. 1 a–f. Hard X-ray (16–30 keV) images (HXIS fine field of view) superposed on Hα images of the flaring (SB) arch of 6 November, 1980 obtained at the Big Bear Solar Observatory. Solar limb is indicated by a dashed line, boundaries of the HXIS field of view by full lines. North is up and west to the right. The brightest contour level in the X-ray images is 90% of the maximum flux F_M; the other contours, 2, 3, ..., n, represent $F_M/2^{n-1}$. Each X-ray plot is an integration of 7 HXIS images over 58 s so that its mean time given in Figures 1(a–f) is $t(X) \pm 29$ s*.

* Because only one of the two HXIS microprocessors was active in November 1980, everywhere in this paper an integration time t means only 0.5 t of real X-ray counting.

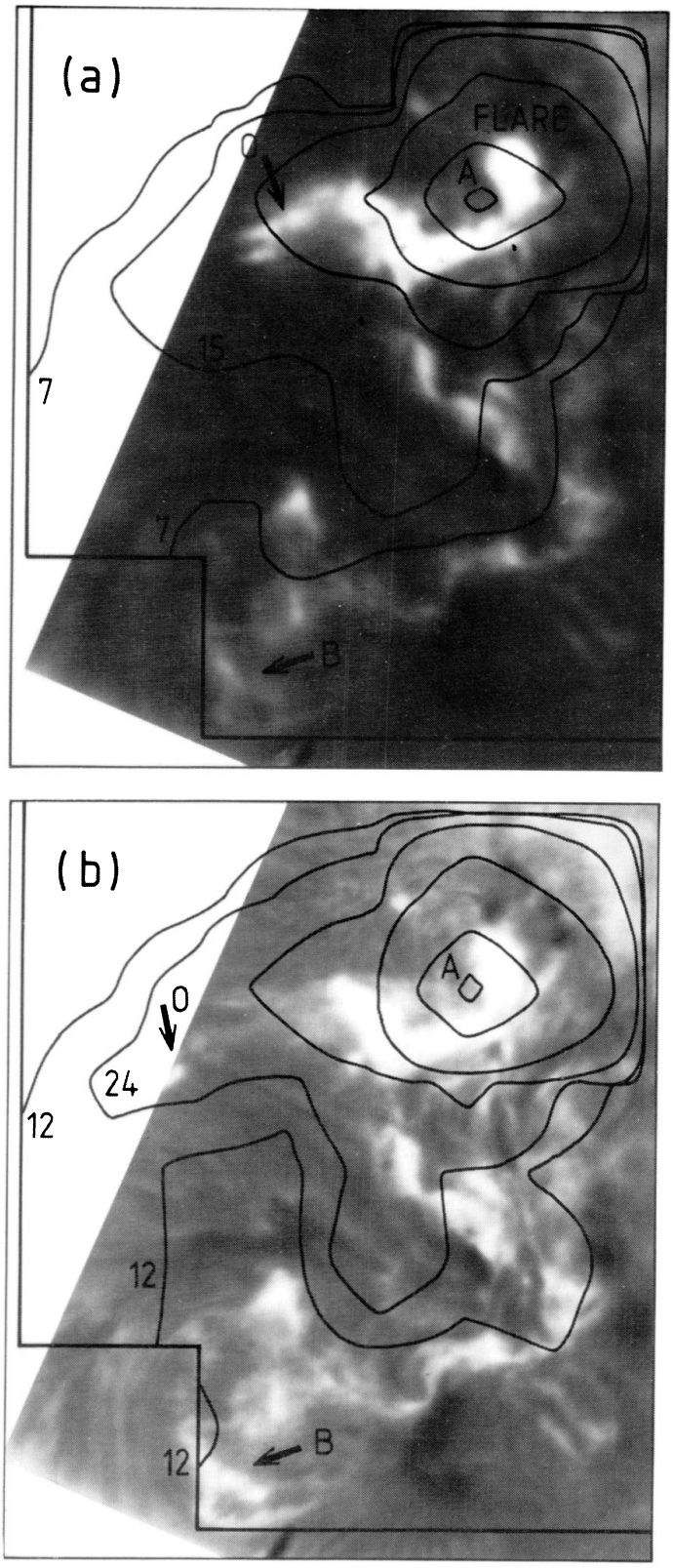

Fig. 2. Soft X-ray (3.5–5.5 keV) images (HXIS coarse field of view) superposed on Hα images of the flaring (L) arch of 12 November, 1980 obtained at the Big Bear Solar Observatory. Boundaries of the HXIS field of view are shown in the figure. East is up and north to the right. Each X-ray plot is an integration of counts over 46 s so that its mean time given in Figures 2(a–d) is $t(X) \pm 23$ s. Total count numbers are shown for the different contours. The lowest contours correspond to 0.30 (a), 0.52 (b), 0.35 (c), and 0.55 (d) counts per second.

Fig. 2a–b. Ejection from the primary footpoint (marked A): (a) $t(H\alpha) = 17:02:49$ UT, $t(X) = 17:02:43$ UT; (b) $t(H\alpha) = 17:04:17$ UT, $t(X) = 17:04:16$ UT. Arrow O points to the

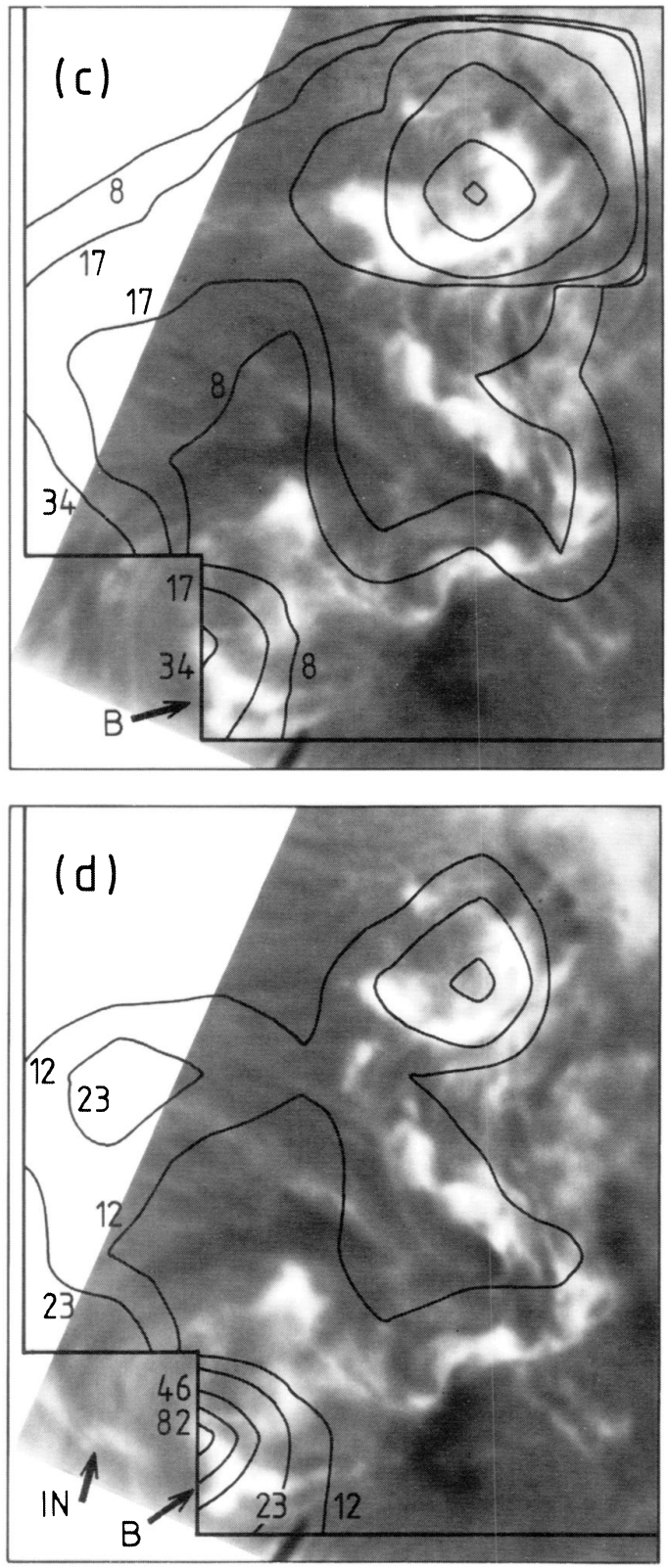

Fig. 2c–d. Inflow into the secondary footpoint (marked B): (c) $t(\mathrm{H}\alpha) = 17:05:46$ UT (note the brightening at B), $t(\mathrm{X}) = 17:05:49$ UT; (d) $t(\mathrm{H}\alpha) = 17:12:36$ UT (arrow IN points to the Hα inflowing mass), $t(\mathrm{X}) = 17:12:33$ UT.

TABLE I

Apparent speeds* of the Hα flow in the flaring arches of 6 and 12 November, 1980

November 6[a]			November 12		
Time (UT)	Distance (km)	Speed (km s^{-1})	Time (UT)	Distance (km)	Speed (km s^{-1})
17 : 26 : 00	11 880	> 290	Fast component[b]		
17 : 27 : 00	26 100	184	17 : 01 : 11	8 500	270
17 : 28 : 00	35 460	128	17 : 02 : 14	26 000	285
17 : 29 : 00	42 240	98	17 : 03 : 17	44 500	306
17 : 30 : 00	47 400	74	17 : 04 : 19	67 500	435
17 : 31 : 00	51 300	56	17 : 05 : 21	93 500	397
17 : 32 : 00	54 210	41	17 : 06 : 24	123 500	561
17 : 33 : 00	56 220	26	17 : 07 : 26	151 500	338
			Slow component[c]		
			17 : 06 : 24	103 300	241
			17 : 09 : 47	153 700	254
			17 : 12 : 54	204 000	295

* The speeds determined for the SB arch are probably close to the real velocity because the arch was near the limb and thus nearly in the plane of the sky. In the L arch, however, the speeds in the legs could be underestimated if the arch was significantly inclined with respect to the plane of the sky.

[a] The speed is averaged over 60 s intervals. The mean time of each such interval is given.

[b] The speed is averaged over 62 s intervals. The mean time is given.

[c] The speed is averaged over 188 s at 17 : 06 : 24, 219 s at 17 : 09 : 47, and 154 s at 17 : 12 : 54. The mean time is given.

the Hα flow could reflect a combination of the ejection speed and the time of the plasma cooling. The induced error, however, should not be large: the plasma density was high near the primary footpoint (Section 4.2) so that the cooling there was a matter of tens of seconds.

During the SB event no images were recorded in the wings of the Hα line and hence we have no information about possible Doppler velocities. (The flow was nearly parallel to the solar limb so that the radial velocity component must be small.) However, in some other events, in particular in the series of the L arches, a few offband images at ± 0.5 Å and ± 1.0 Å clearly show the ejected material near the primary footpoint to be Doppler-shifted into the blue wing during the ejection phase. Sometimes material is even seen falling back and red-shifted in the late phase of the events.

3.2. Confinement and Fine Structure

There is no indication that the arch system changes shape or size during the mass flow and flaring (i.e., it does not expand, grow, contract, or shrink). As Figure 1 demonstrates quite clearly, the flaring arch consists of a large number of fine threads which have apparent dimensions of 1–5 arc sec (and might be composed of still finer unresolved structures). The observed threads are of different Hα brightness and thus presumably different densities. Similar fine structure could be present in the X-ray emission as well,

but the HXIS spatial resolution (of 8 arc sec in Figure 1 and 32 arc sec in Figure 2) does not allow its detection. Other minor flaring-arch events in the same system, preceding or following the major event, sometimes occur in strands which are lower or higher than in the major arch (cf. Paper II). Apparently only a part of the coronal arch is activated at a given time, and different parts are affected at different times.

3.3. Propagating X-ray emission

In X-ray images one can also see the emission propagating through the same system of arches as the Hα material (which, however, need not necessarily imply that the same individual loops are affected in Hα and X-rays). This propagation is faster than in Hα as one can very well see in Figure 1 for the SB arch and in Figure 2 for the L arch.

Details about the X-ray propagation through the L arch can be deduced from the time-evolution map in Figure 3. Times of the onset (the leading edge) and of the maximum of the X-ray (>3.5 keV) emission at different spatial positions within the arch are plotted in Figure 4. The leading edge of the X-ray emission moved first slowly (with ~ 360 km s^{-1}) through the arch and its speed abruptly increased, at about 85 000 km from the primary footpoint, to ≈ 1640 km s^{-1}. Although there is large scatter of the measured points, the sudden increase in speed is clear. In contrast to that, the position of maximum X-ray emission propagated along the first $\approx 85\,000$ km with a high speed > 1100 km s^{-1} (and possibly much faster: note that there is very little change in the time of maximum flux below 85 000 km). After distance of 85 000 km, the speed abruptly decreased to about 480 km s^{-1}.

The interpretation is that there was first a slow ejection starting between 16 : 58 and 16 : 59 UT followed by a second, very fast ejection at 17 : 01 UT (cf. the extrapolations in Figure 4). The fast component overtakes the slow component at a distance of 85 000 km. Before that we see the slowly moving leading edge of the first component, after that the rapidly moving edge of the fast component. But the slower component is still measurable from the propagation of its maximum flux, because the flux of the fast component decreases more rapidly.

The HXRBS time profile is shown in the left side of Figure 4 for comparison with the fast and slow components detected by HXIS. The extrapolated beginning of the fast component in the arch at 17 : 01 : 00 UT corresponds closely in time with the beginning of the steep rise of the hard X-ray burst to maximum. The fast decay of the maximum flux in the arch indicates that also the duration of the fast component corresponds to the duration of the HXRBS burst.

If the speed of the slow component is 480 km s^{-1} as shown in Figure 4, the start of this ejection from the primary footpoint would be at 16 : 58 : 50 UT and of the fast one at 17 : 01 : 00 UT. Though the assumption of a constant speed of propagation makes these times somewhat uncertain, they agree well with the Hα onset times in Section 3.1.

This event was also studied by Rust, Simnett, and Smith (1985) together with seven other cases of 'fast moving fronts'. Two of the events they list were flaring arches (the same ones we discuss here), but the remaining five were not (i.e., Hα photographs do not show any plasma flow and X-ray characteristics are different). Rust, Simnett, and

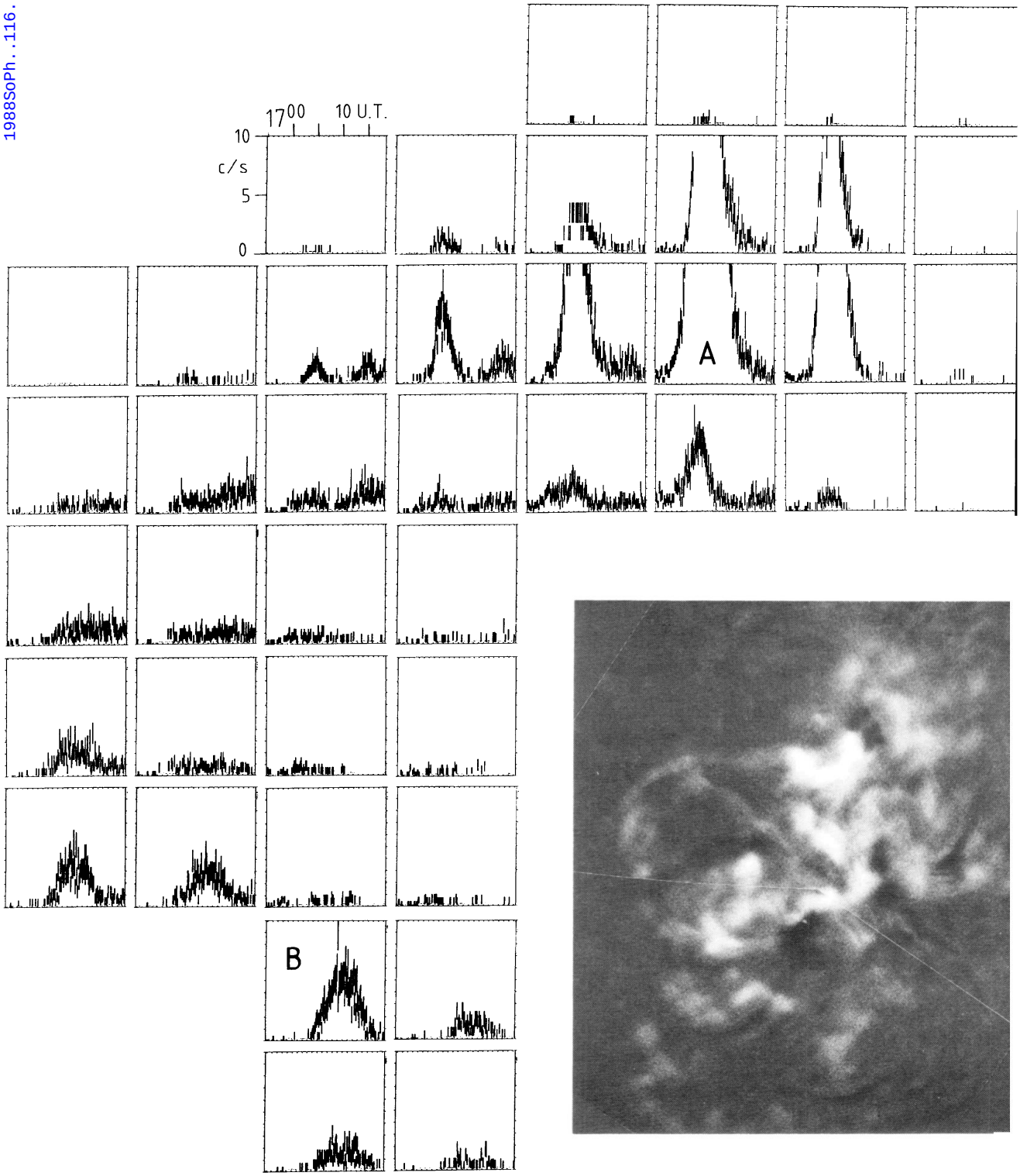

Fig. 3. Time-development map of the flaring (L) arch of 12 November 1980. Every pixel of the coarse field of view of HXIS shows the time development of >3.5 keV flux within the area of 32×32 arc sec it images. Time (16 : 55–17 : 18 UT) is on the abscissa, X-ray flux (0–10 counts s^{-1}) on the ordinate. The arch footpoints are in the pixels A and B (though the secondary footpoint might be also located slightly to the left of pixel B, out of HXIS field of view.) East is up, north is to the right. Figure 4 is based on these plots, assuming that the X-ray arch trajectory was the same as the arch seen in Hα.

Insert: a combination of two segments of Big Bear full-disk Hα photographs (at 17 : 07 : 27 UT and 17 : 15 : 27 UT) which makes the whole arch structure visible.

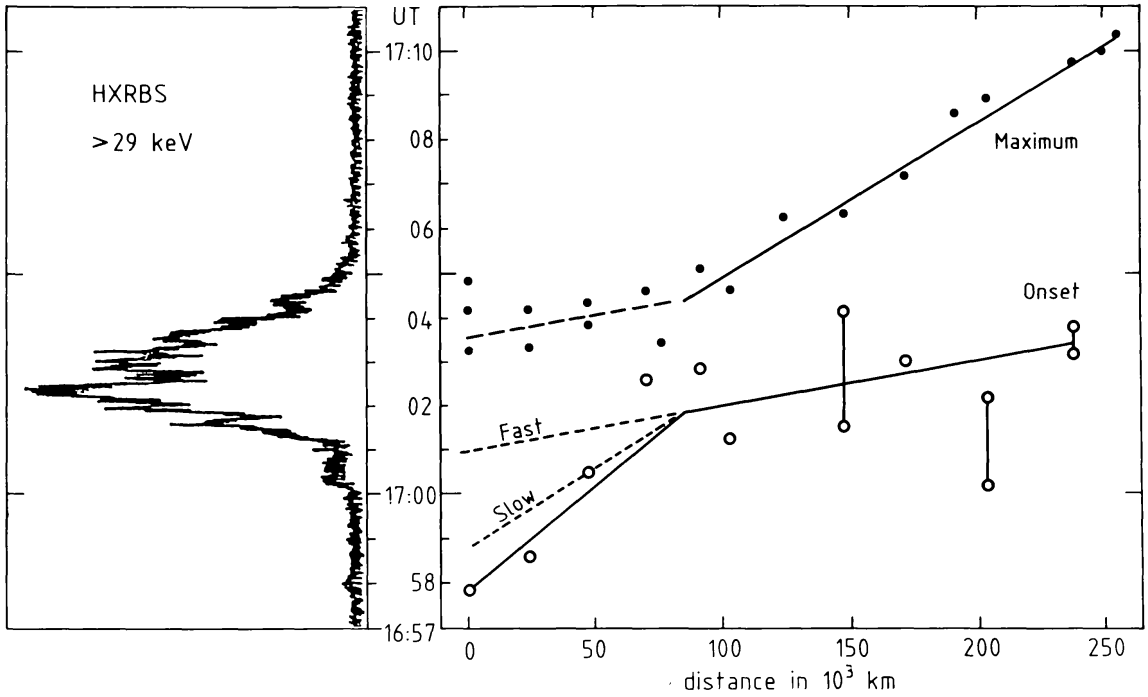

Fig. 4. Plot of the time of the onset (circles) and maximum (dots) of the >3.5 keV X-ray enhancement at various positions of the flaring (L) arch of 12 November, 1980. The distance in 10^3 km from the supposed origin of the excitation (the primary footpoint) is on the abscissa, UT is on the ordinate. Full lines show the best approximation to the measured points; the long-dashed line is the minimum speed corresponding to maxima prior to 17 : 04 UT (but note that even an infinite velocity would fit the data well). The short-dashed lines are extrapolations of tentative fast and slow ejections (cf. text), under the assumption of constant speeds. Adjacent to the time scale is the Hard X-Ray Burst Spectrometer record of >29 keV hard X-rays (courtesy of Brian Dennis) to demonstrate the coincidence of the onset of the hard X-ray burst and the fast ejection.

Smith followed the displacement of the 8.0–16 keV emission along the L arch and found a front velocity of 925 km s^{-1} between 17 : 01 and 17 : 06 UT. Fárník (private communication) repeated the same analysis for 8.0–11.5 keV X-rays; he found the counts in the 8.0–11.5 keV band to be lower by an order of magnitude than the counts in the 3.5–5.5 keV band. Thus we believe that our speeds, based on 3.5–5.5 keV X-rays with significantly better statistics, are more reliable and correct. (Note that Rust, Simnett, and Smith misidentified the location of the secondary Hα footpoint in their Figure 5.)

In the SB arch we were unable to measure the X-ray propagation along the arch: at high energies (as those plotted in Figure 1) the statistics of the counts were insufficient in individual (non-integrated) images; at lower energies a preheating (seen, e.g., in Figure 5) masked the following propagation of the exciting agent. See, however, Section 3.9 for additional information: the mean propagation speed can be estimated to be 1070 km s^{-1}.

3.4. Chromospheric flare at the primary footpoint

Both flaring arches were associated with chromospheric flares at their primary footpoint. In the SB arch this chromospheric component (a subflare) consisted of two very small Hα patches (not resolved but visible as one bright patch in Figure 1; they are

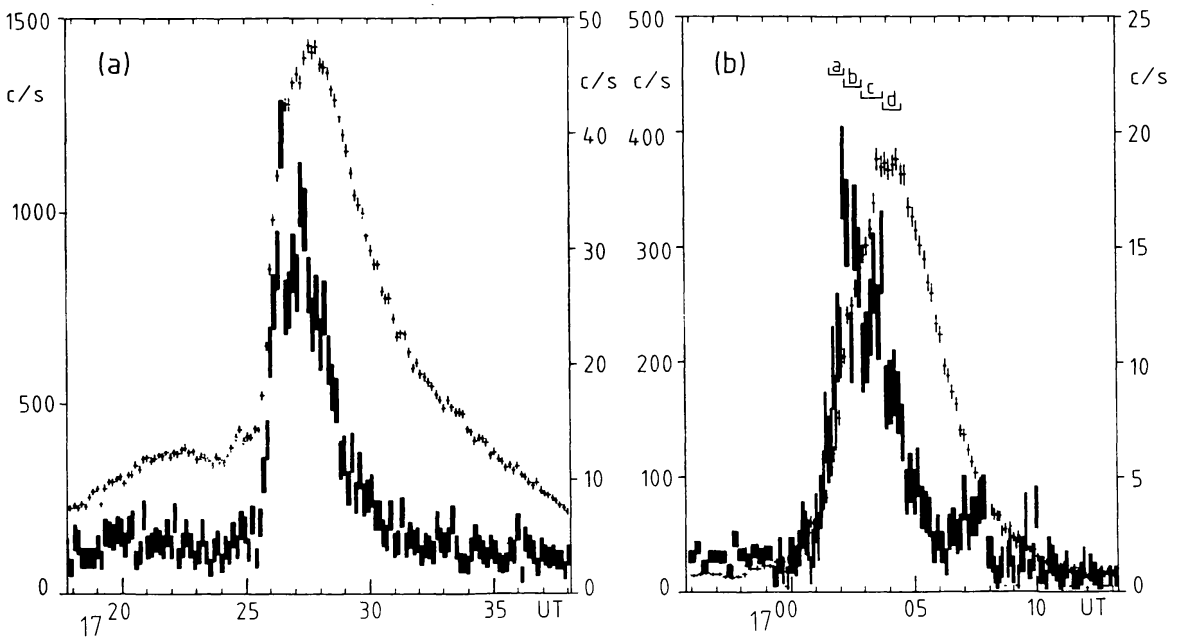

Fig. 5. Soft X-ray (3.5–5.5 keV) bursts (crosses, left scales) and hard X-ray (16–30 keV) bursts (bars, right scales) observed by HXIS at the onset of the flaring arches of (a) 6 November, 1980 (SB) and (b) 12 November, 1980 (L). The height of the bars or crosses corresponds to $\pm 1\sigma$ deviations, their width to the length of the exposure time of individual HXIS images. Total counts per second in the fine field of view of HXIS are given on the scales. Horizontal bars in (b) refer to the integration times of the images in Figures 6 (a–d).

well resolved in D_3 line images of He I). In the L arch, however, the associated chromospheric flare was quite extensive (of Hα importance 1B) forming a semi-circular pattern around the tentative site of the mass ejection (Figure 2). This flare was studied in detail by NacNeice *et al.* (1985). Though they noticed the existence of material flowing from the flare site to the secondary footpoint (marked by *W* in their Figure 1), they did not pay any more attention to this phenomenon. Thus it is evident that the flaring arch is not the flare itself but rather it is a component of a complex flare phenomenon.

3.5. X-RAY BURSTS

Figure 5 shows the hard (16–30 keV) and soft (3.5–5.5 keV) X-ray bursts observed by HXIS in the onset phase of the two discussed flaring arches. Very similar hard X-ray bursts were also recorded by the Hard X-Ray Burst Spectrometer on board the SMM (HXRBS – Orwig, Frost, and Dennis, 1980) in the energy range 29–58 keV: the HXRBS maximum flux was 1236 counts s^{-1} in the SB arch and 653 counts s^{-1} in the L arch (Dennis *et al.*, 1985). The HXRBS burst for the L arch can be seen in Figure 4, and for the SB arch the burst was shown by Švestka *et al.* (1983) in their Figure 4.

These X-ray bursts have unique characteristics: their rise is extremely steep, they are unusually long-lived at high energies, but their duration is only slightly longer at lower energies. In the majority of flares, the soft X-ray burst has a much slower and longer decline than the hard burst; compare e.g., the duration of the 3.5–5.5 keV emission from the SB arch with another flare preceding it at 14 : 44 UT (both of Hα importance 2) in

Figure 2 of Švestka (1984). Clearly, the duration of the X-ray burst of a flare with a flaring arch is anomalously long in hard X-rays and/or anomalously short in soft X-rays. This is such a typical characteristic that other flaring arches could be discovered just by checking the X-ray records of HXIS (cf. Paper II and planned later papers in this series).

3.6. Radio emission

No radio burst was reported in *Solar Geophysical Data* at the time of the SB arch, but a burst was recorded at 10.6 GHz at the Owens Valley Radio Observatory although the rise phase was missed due to instrument calibration. At the onset of the L arch, a single burst from 1.4 through 15.4 GHz was reported starting at 16 : 59.6 UT (*Solar Geophysical Data*, 1981b). A significant burst was also recorded at 10.6 GHz at Owens Valley from 17 : 00 UT until an interruption in the observations at 17 : 58 UT. The main phase, which lasted about 9 min, was preceded by an onset phase in the interval from 16 : 55–17 : 00 UT (G. Hurford, private communication). The duration and shape of the main phase of the microwave burst was very similar to the X-ray burst above 3.5 keV shown in Figure 5(b).

3.7 Timing of the hard X-ray burst

As Figure 4 demonstrates, the fast ejection in the L arch coincided exactly with the onset of the hard X-ray burst at 17 : 01 UT. This happened two minutes or more after the onset of the first (slow) ejection of the Hα material into the flaring arch and the soft X-ray and microwave pre-heating of the lower part of the arch.

In the SB event, the ejection of plasma into the arch also coincides, within the range of uncertainties in timing, with the onset of the hard X-ray burst. The isophotes superposed on the Hα images in Figure 1 are images of the hard (16–30 keV) X-ray burst and nicely show the burst time development. This kind of imaging could not be done for the L arch which was observed in the coarse field of view of HXIS with lower sensitivity. However, at least the primary footpoint (i.e., the flare, cf. MacNeice *et al.*, 1985) could be imaged in the fine field of view. The imaging (Figure 6) shows that various

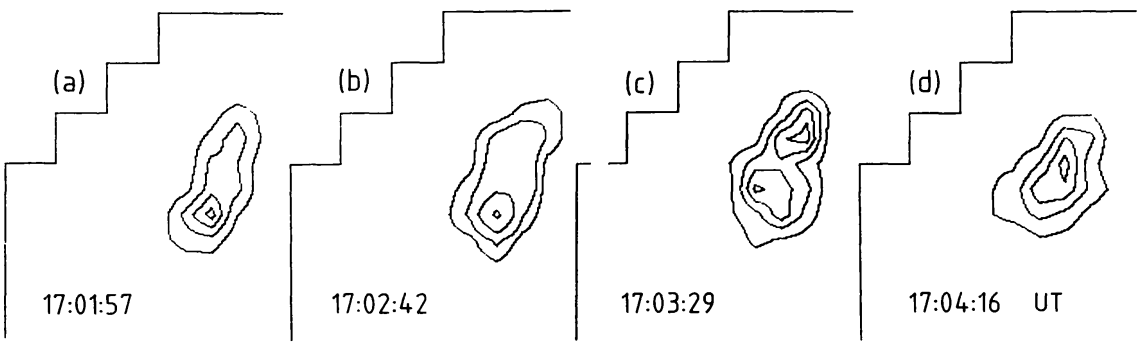

Fig. 6. Hard X-ray (16–30 keV) images of the primary footpoint of the L arch of 12 November, 1980. Integration time: (a) 40 s, (b) 42 s, (c) 60 s, (d) 42 s. Maximum and minimum contours (counts s^{-1}): (a) 24, 6; (b) 34, 4; (c) 24, 6; (d) 14, 7. Mean UT time of the integration is given in every image (compare with Figure 5(b)).

parts of the hard X-ray burst originated at different positions. Also the main two components of the burst, seen in Figure 5 at approx. 17 : 02 : 30 and 17 : 04 : 00 UT, occurred at two slightly different positions some 15–20 arc sec apart. Thus, the ejecta in various elementary threads of the arch system apparently originated at slightly different times; in particular, one can identify two subsequent large ejections from two different sites, separated by approximately 10000 km in space and by 1.5 min in time.

Note that a double X-ray peak can be detected in the SB arch as well: cf. Figures 5(a) and 8(a). The spiky character of the hard X-ray bursts, the fine structure of the SB arch, and varying speeds of Hα knots of emission in this arch indicate that the events may represent a series of elementary injections into the arch system.

3.8. Brightening of the secondary footpoint in Hα

Figure 7 shows photometric tracings of the Hα emission at the secondary footpoint of the L arch, compared with the hard X-ray burst at the primary footpoint. It is seen that the Hα chromosphere began to brighten at the secondary footpoint as soon as the hard X-ray burst set in. The maximum possible delay is 40 s which would yield $v > 6575$ km s^{-1} for the speed of the exciting agent propagating along the arch. But

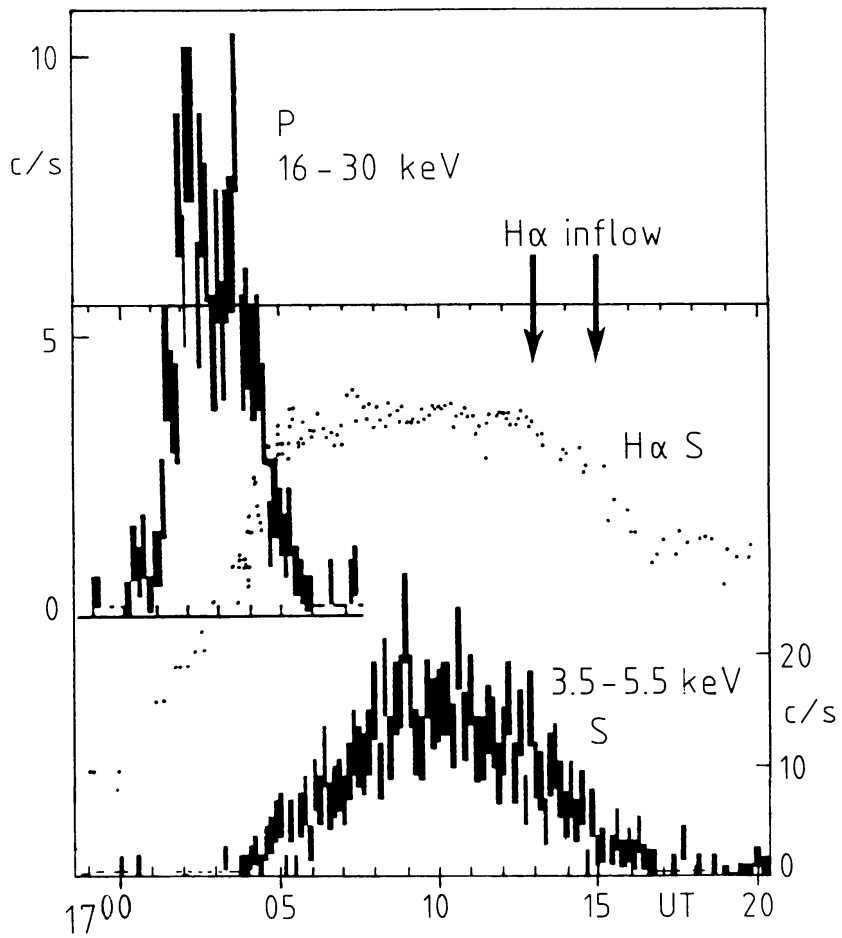

Fig. 7. Relative photometry of the Hα brightness in the secondary footpoint of the L arch (dots) compared with the hard (16–30 keV) X-ray burst in the primary footpoint (*P*) and with the soft (3.5–5.5 keV) X-ray burst in the secondary footpoint (*S*).

more likely the time difference is a matter of a few seconds: a delay of 5 s would yield $v > 52\,600$ km s^{-1}.

In the SB arch the secondary footpoint brightened in Hα slightly during the precursor (Figure 8(a)) and this makes the determination of the real onset time difficult. If there is any time difference between the X-ray burst and the onset of the intense Hα brightening, then the Hα even preceded the X-rays. Hence, again, the real time difference seems to be of the order of seconds.

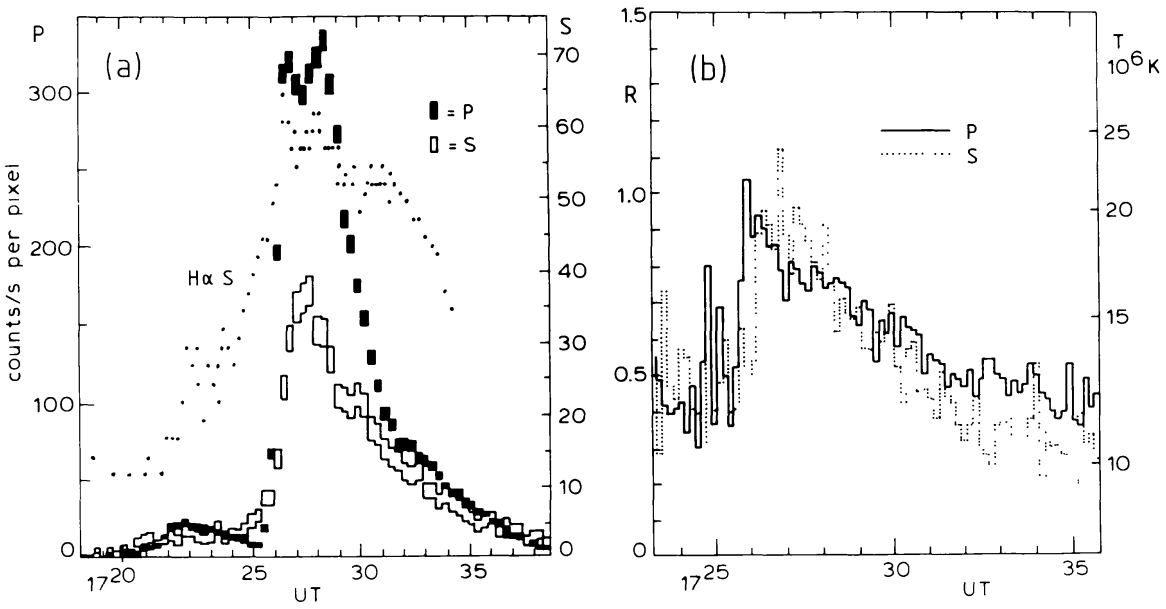

Fig. 8. (a) Relative photometry of the Hα brightness in the secondary footpoint of the SB arch (dots) compared with the soft (3.5–5.5 keV) X-ray bursts in the primary (P) and secondary (S) footpoint. Note that the scales for P and S are different. (b) The flux ratio of the 5.5–8.0 and 3.5–5.5 keV energy bands of HXIS in the primary (P) and secondary (S) footpoints of the SB arch. The corresponding temperature (under assumption of purely thermal emission, cf. Mewe *et al.*, 1985) is given as the right-hand scale.

3.9. Brightening of the Secondary Footpoint in X-rays

In contrast to the Hα emission, the response of the secondary footpoint in X-rays is not an immediate increase in brightness as one can see in Figures 7 and 8.

In Figure 8(a) we compare the 3.5–5.5 keV emission in the two pixels of HXIS fine field of view which had the highest number of counts in the primary and secondary footpoints of the flaring arch SB. The time difference between the X-ray excitation of the two footpoints is still better defined if one compares their temperatures instead of counts, as we have done in Figure 8(b). There one can see that the secondary footpoint began to be enhanced in X-rays 29 $\pm$ 5 s after the primary footpoint. This corresponds to a propagation speed $v = 1965 \pm 340$ km s^{-1}. The time difference between X-ray maxima, at the primary and secondary footpoints, was 53 $\pm$ 10 s which can be interpreted as mean propagation speed of 1070 $\pm$ 200 km s^{-1}.

In Figure 7, for the L arch, we show the time variation of 3.5–5.5 keV X-rays in the

HXIS coarse-field-of-view pixel marked B in Figure 3 in comparison with the hard X-ray brightening at the primary footpoint. In this pixel of the L arch, a clear rise in X-rays starts only 2^m45^s after the onset of the hard X-ray burst. This corresponds to $v = 1594$ km s^{-1}. The time difference between X-ray maxima was 7^m30^s, which can be interpreted as a mean propagation speed of 584 km s^{-1}.

The velocities deduced from the onset times may be incorrect if the longer delay time is simply due to a lower sensitivity in X-rays than in Hα: a certain minimum flux level must be reached before HXIS begins to record counts; then a fictitiously late onset in X-rays would be indicated in spite of the fact that the rise actually began earlier. This effect, however, does not affect the time difference of the maxima so that the mean propagation speed is well defined.

3.10 X-RAY SPECTRUM IN THE SECONDARY FOOTPOINT

HXIS imaging of the footpoints of the SB arch at different energies has revealed that the X-ray spectrum was harder in the secondary footpoint than in the primary one. The ratio of the 16–30 keV flux over 3.5–5.5 keV flux at the time of the maximum flux at the two footpoints was 0.037 ± 0.003 and 0.073 ± 0.012 at the primary and secondary footpoint, respectively (Figure 9(c)). The ratio between the secondary and primary footpoint maximum countrate was 0.112 ± 0.003 at 3.5–5.5 keV, but 0.313 ± 0.090 at 16–30 keV. In other words, the fictitious temperature corresponding to the ratio of hard-to-soft X-rays was lower in the primary source of heating than in the point where

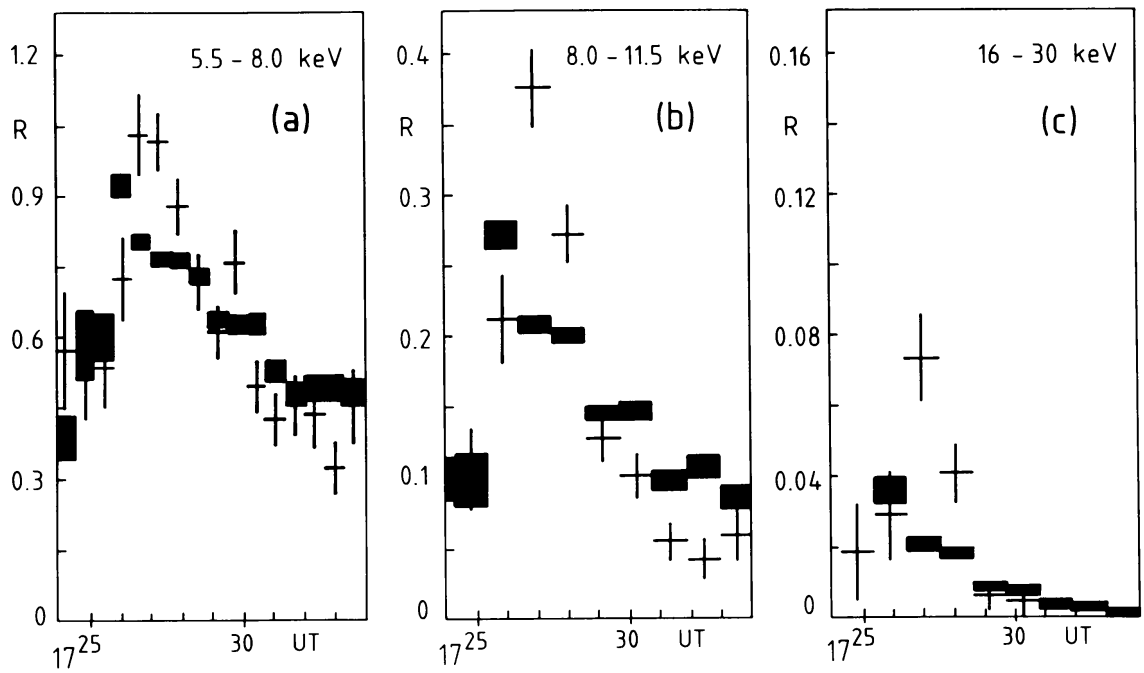

Fig. 9. Ratios of counts in different energy bands of HXIS in the primary (bars) and secondary (crosses) footpoint of the SB arch. Counts in the pixel with maximum flux were summed in each footpoint, the accumulation time was 60 s. (a) 5.5–8.0 keV/3.5–5.5 keV. (b) 8.0–11.0 keV/3.5–5.5 keV. (c) 16–30 keV/3.5–5.5 keV.

the heat was transported. This heating anomaly is confirmed in Figure 9 which shows the time variation of the HXIS count ratios between different energy bands in the two footpoints. The higher is the energy of the band, compared with the lowest energy band of 3.5–5.5 keV, the larger is the difference between the ratios (and thus fictitious temperatures) in the footpoints.

We will see in Paper II that also other flaring arches at the site of the SB arch, which could be fully imaged in the fine field of view of HXIS, show this temperature anomaly. The relative hardness of the spectrum is most pronounced when only the two brightest pixels at the footpoints are compared. When more pixels are integrated, the effect is smeared and becomes less impressive, but still does exist for four integrated pixels at each site. Since, however, one pixel of HXIS coarse field of view corresponds to an integration of 16 pixels of the fine field of view of HXIS, the spectral hardening, even if it were present, cannot be checked in the images of the L arch. Besides, a significant portion of the secondary X-ray footpoint of the L arch might have been situated outside the HXIS field of view (cf. Figure 3).

3.11 The aftermath phase

As already shown by Rust, Simnett, and Smith (1985), the L arch exhibited an aftermath phase when soft X-ray emission was seen to intensify again in the leg of the arch above the primary footpoint (cf. Figure 7 in Rust, Simnett, and Smith and the secondary maximum peaking around 17 : 15 UT in our Figure 3). From the X-ray pictures alone it is difficult to decide whether this brightening represents a new outflow or inflow of mass or a stationary heating. However, reverse flow was subsequently seen in Hα in this leg from 17 : 14 to 17 : 35 UT. Since the inflow of Hα material into the secondary footpoint occurs at about 17 : 13 UT, this reverse flow near the primary footpoint is seen almost immediately after the outflow is no longer obvious. It might be a new injection of which most material falls back. If not, then the reverse flow must begin many minutes before the outflow ceases, because the Hα flow is relatively slow. It is apparent in the Hα time-lapse film that at least part of the reverse flow appears to be in threads adjacent to (below) the site of the initial Hα outflow. Thus the reverse flow does not necessarily follow precisely the same field lines as the initial injection.

Even later on, after its flaring and the aftermath phase, the arch was still subject to variable weaker activity in X-rays.

3.12 Chronological summary of changes observed in flaring arches

Although the main phase of X-ray and Hα mass flow through the arches is the most obvious signature of them, the entire event of a flaring arch consists of three, and sometimes four, distinct consecutive phases. As we will see in Section 4, the distinction between these phases is not only morphological: they also correspond to different ranges of temperature and density and possibly even to different processes that produce them.

These phases are as follows:

(1) The Early Phase: brightening of the secondary footpoint in Hα within a few seconds of the start of the hard X-ray burst at the site of the primary flare. This phase

is similar to the peripheral or remote flare brightenings described by Rust and Webb (1977), Martin (1979), Tang (1982), and Duijveman, Hoyng, and Machado (1982).

(2) The Main X-Ray Phase: propagation of X-ray emission through the arch from a primary footpoint in the source flare to the secondary footpoint; appearance of the secondary footpoint in X-rays; further brightening of the secondary footpoint in Hα. The X-ray spectrum appears harder in the secondary, than in the primary, footpoint.

(3) The Main Hα Phase: propagation of Hα-emitting mass through the same arch following the X-rays; inflow of the Hα-emitting mass into the secondary footpoint, while the brightness at the secondary footpoint begins to decline.

(4) The Aftermath Phase: faint Hα emission, associated with soft X-ray brightening, sometimes is seen flowing in the reverse direction in the primary leg of the arch.

In the next section we will try to suggest an interpretion of at least some of these typical characteristics of the phenomenon of flaring arches.

4. Discussion

4.1. Overview

We do not presume that a complete interpretation of flaring arches can be made on the basis of limited observations of two events observed in just two parts of the electromagnetic spectrum. However, these observations are extensive enough to guide the direction of theoretical investigations. As a starting point to the discussion we list below the key observations which any theoretical interpretation of flaring arches should take into consideration:

(1) The Hα brightening at the secondary footpoint of the arch begins before either the Hα emission or X-ray emission is seen to travel through the arch.

(2) However, a sharp increase of this Hα brightening coincides with the onset of the X-ray emission at the secondary footpoint and there is general agreement between the maxima and decline of the Hα light curve and the X-ray emission curve at the secondary footpoint (cf. Figures 7 and 8(a)).

(3) There is no increase in the Hα emission at the secondary footpoint at the time when the Hα emission flow arrives there. (This time is marked 'Hα inflow' in Figure 7.)

(4) The duration of emission at the primary and secondary footpoints and in the arch is similar in both Hα and X-rays.

(5) The difference in duration of the hard and soft X-ray bursts is unusually small (Figure 5).

(6) The X-ray spectrum at the secondary footpoint is harder that at the primary site of the ejection (at least in the SB arch).

(7) There is a wide spectrum of propagation speeds as deduced from the Hα brightening at the secondary footpoint, X-ray brightening of the arch, and Hα flow through the arch, respectively.

(8) Hα images show clearly a fine structure in the arch.

(9) There must be very large differences in temperature and density within the arch

structure: from $\sim 10^7$ K and coronal densities in the X-ray-emitting plasma to $\sim 10^4$ K and chromospheric densities in the material emitting in Hα.

Some of the physical implications that can be derived from these key observations are discussed in the following sections.

4.2. Hα AND X-RAY EMISION AT THE SECONDARY AND PRIMARY FOOTPOINTS

The almost immediate brightening of the secondary footpoint in Hα is substantial evidence of the propagation of a population of energetic electrons through the arch within a few seconds of the start of the hard X-ray burst at the primary footpoint. This early Hα brightening is similar to remote brightenings previously observed and previously interpreted as being due to the impact of electrons on the chromosphere.

The absence of a corresponding X-ray brightening for tens of seconds (in the SB arch) or minutes (in the L arch) is probably due to the threshold of HXIS and indicates that there were not enough electrons with energy in excess of 3.5 keV in the initial streams. Thus either the electron energy spectrum was very soft or the electron density population was low.

Equally noteworthy is the absence of any increase in the Hα brightness at the secondary footpoint upon the arrival of the Hα emitting mass. According to Fontenla an Machado in Švestka *et al.* (1987) and Heinzel and Karlický (1987) an Hα loop projected on the solar disk can appear in emission only if its internal pressure exceeds ≈ 1–3 dyn cm^{-2}. For the temperatures at which the Hα line is formed this requires $n_e \geq 5 \times 10^{11}$ cm^{-3}, a fact already suspected earlier by Zirin (1987). A motion along the line-of-sight can increase this limit density, but it cannot reduce it. Therefore, the falling mass had a density close to the density of the chromosphere and we see here evidence that the kinetic energy of free-falling mass as dense as the chromosphere was insufficient to cause any detectable chromospheric brightening. This sets a rather high lower limit to the energy of the associated processes producing this emission at the secondary footpoint.

When comparing the Hα and X-ray emission at the secondary footpoint in Figure 7, we note three main features: (1) an increase in the slope of the Hα emission coincident with the beginning of the X-ray emission: (2) a close correspondence between the decline of X-ray emission and Hα emission; and (3) a similar duration for the X-ray and Hα maxima. Therefore, Figure 7 along with Figure 8a provides evidence that the more intense core of the Hα emission and all of the X-ray emission at the secondary footpoint are caused by the same physical process.

We now ask whether that process is just an increase in the flux of electrons which caused the initial Hα brightening, or whether it is another process which replaces the initial electron energy deposit in the chromosphere. At least for the SB arch, the greater spectral hardness at the secondary footpoint, demonstrated in Section 3.9 and Figure 9, supports the idea that the energy is transported by particles. The difference in spectral hardness of the footpoints (demonstrated for more events and in more detail in Paper II) is most likely due to energy-dependent energy losses in particle streams which excite X-rays at the secondary footpoint: as fast electrons stream along the arch from the

primary footpoint, those with lower energy suffer heavier losses than the more energetic ones so that the impinging electron stream hardens. The difference in spectral hardness may be further enhanced by a greater abundance of soft thermal emission of the flare near the primary footpoint, but this again implies that the emission at the secondary footpoint is nonthermal, i.e., due to particle streams.

An electron above 3.5 keV spiralling aroud a field line would need less than 4 s to traverse the SB arch and less than 15 s to complete its travel along the L arch. This is in agreement with the observed time delays of the initial Hα brightening at the secondary footpoints. Also the core of the SB arch could be caused by electrons, as the primary and secondary emissions were essentially contemporaneous (Figure 8). (The initial delay in X-rays will be discussed in Section 4.6.) However, as Figure 7 shows, the core of emission at the secondary footpoint of the L arch peaked as late as several minutes after the end of the hard X-ray burst (i.e., the period of particle release) at the primary source of energy. Thus electrons can not be responsible for the emission at the secondary footpoint of the L arch.

In the L arch we have no evidence that the energy spectrum hardened so that particle streams need not be responsible for the core emission. Rust, Simnett, and Smith (1985) suggested a fast-moving thermal conduction front as the source of the gradual excitation of the core (cf. Section 4.6). However, one might also tentatively consider proton streams as an alternative. Protons of the same energy as electrons require about 40 times more time to traverse the arches. Thus the first brightening in Hα cannot be due to protons because they would arrive too late; but arrival of protons would not be inconsistent with the further increase of Hα brightening at the time of the onset of the X-ray emission above 3.5 keV at the secondary footpoint. The travel time of 3.5 keV protons through the L arch would exceed 5.4 min.

4.3. Patterns of Temperature and Density in the Arches

To investigate whether the X-ray emission above 3.5 keV at the secondary footpoint of the SB arch could be entirely due to electrons propagating through the arch, we estimate the energy losses in the arch for various densities assumed within the arch.

Excitation of a secondary footpoint through electrons was discussed by Duijveman, Hoyng, and Machado (1982) in a flare loop that occurred one day prior to the SB arch in another active region. The streaming electrons lose their energy predominantly through Coulomb collisions. Due to Coulomb interactions with plasma of density $n_e(l)$ the original energy of an electron, $E(0)$, will decrease to $E(s)$ after passing the path s:

$$E^2(s) \simeq E^2(0) - 5.3 \times 10^{-18} \int_0^s n_e(l)\, \mathrm{d}l\,, \tag{1}$$

with $E(0)$ and $E(s)$ in keV. Let us (considering the SB arch) put $s = L$, where L is the lenth of the arch. In order to produce X-ray emission in the 3.5–5.5 keV or 16–30 keV energy range, the impinging particle energy $E(L)$ must exceed 3.5 or 16 keV, respectively. Let us further suppose that the plasma density, n_e, is independent of l. Then Table II

TABLE II

Minimum electron energies, $E_m(0)$, at the acceleration site required to produce >3.5 or >16 keV X-rays or the Hα emission at the secondary footpoint of the SB flaring arch, in dependence on the arch density (assumed constant)

n_e	$E_m(0)$		
	≥3.5 keV	≥16 keV	Hα
10^{12} cm^{-3}	174 keV	175 keV	174 keV
10^{11}	55.1	57.3	55.0
10^{10}	17.7	23.6	17.4
10^{9}	6.52	16.9	5.50
10^{8}	3.91	16.1	1.74

gives the minimum energies $E_m(0)$ required by Equation (1) for $E(L) \geq 3.5$ keV and $E(L) \geq 16$ keV, respectively, at different constant densities n_e throughout the arch.

One can see from this table that the energy losses stay reasonably low if electrons propagate through densities of the order of 10^9 cm^{-3} or less. In order to make a more exact estimate of the maximum acceptable density, we will use the flux ratios in the primary and secondary footpoint given in Section 3.10.

Under the assumption of a power law,

$$F(E) = \alpha E^{-\gamma}, \tag{2}$$

Dennis (in Švestka *et al.* 1983) found $\gamma \simeq 8$ for the X-ray flux above 29 keV (a very soft spectrum for an event of this intensity).

From HXIS data, 3.5–30 keV, one finds approximately $\gamma \simeq 4$. For a thick-target emission at the footpoints (Brown, 1971; Hoyng, Brown, and van Beek, 1976), the energy flux into the target region, for $E > E_0$, is

$$P(E_0) = f(\gamma) \int_{E_0}^{\infty} F(E)\, \mathrm{d}E = f(\gamma)\, E_0^{-(\gamma-1)}. \tag{3}$$

According to Section 4.9, the ratio

$$P(E_0)_{\text{secondary}}/P(E_0)_{\text{primary}}$$

was 0.11 for $E_{01} = 3.5$ keV and 0.31 for $E_{02} = 16$ keV. The length of the arch ($s = L$ in Equation (1)) was 5.7×10^9 cm. Thus, for constant n_e along the arch, we get the following conditions from Equations (3) and (1):

$$\begin{aligned} (3.5/E_{01})^{\gamma-1} &= 0.1\,, \\ E_{01}^2 &= 3.5^2 + 3 \times 10^{-8}\, n_e\,, \end{aligned} \tag{4}$$

and

$$(16/E_{02})^{\gamma-1} = 0.3\,, \qquad E_{02}^2 = 16^2 + 3 \times 10^{-8} n_e\,. \tag{5}$$

For $\gamma = 4$, in both Equations (4) and (5), one finds $n_e = 1.5 \times 10^9$ cm^{-3} from (4) and $n_e = 1.1 \times 10^{10}$ cm^{-3} from Equations (5).

This difference in the n_e values is apparently due to our approximation of a constant γ. If one takes $\gamma = 3$ in (4) and $\gamma = 8$ in (5), the resulting values of n_e are 3.7×10^9 cm^{-3} for $E_{01} = 3.5$ keV and 3.5×10^9 cm^{-3} for $E_{02} = 16$ keV. Clearly, for a relatively hard spectrum at low energies which softens at high energies (as really was observed), the X-ray emission at the two footpoints can be properly interpreted; the initial density, through which the electrons streamed, should be close to 4×10^9 cm^{-3}.

The deduced density, 4×10^9 cm^{-3}, is well within the range found by Duijveman, Hoyng, and Machado (1982) for other coronal loops of these dimensions. According to Equation (1) (also cf. Table II), the minimum energy $E_m(0)$ required then at the primary footpoint for producing X-rays above 3.5 keV at the secondary end of the SB arch is 11.6 keV. This, however, is a condition that cannot be fulfilled, because the really observed maximum flux above 3.5 keV at the secondary footpoint exceeded by a factor 3 the flux above 11.5 keV at the primary footpoint. Thus the density must have been overestimated in the approximate computations of the preceding section. The fluxes above 3.5 keV at the secondary footpoint and above $E_m(0)$ at the primary footpoint would be equal for $E_m(0) = 8.5$ keV. This, according to Equation (1), requires $n_e = 2.0 \times 10^9$ cm^{-3}. Thus 2×10^9 cm$^{-3} < n_e < 4 \times 10^9$ cm^{-3} seem to be reasonable limits for the SB arch under the assumption that the secondary footpoint emission is all due to electron streams. But even if only the onset brightening in Hα is caused by electrons, the density through which these electrons travel cannot be significantly higher (cf. the last column in Table II).

The same density in the L arch would require $E_m(0) = 19$–22.5 keV for producing > 3.5 keV X-rays at the secondary footpoint. It is quite clear that not enough electrons above 19 keV were produced at the primary footpoint to cause the X-ray emission seen at the secondary end of the arch: in the secondary footpoint (pixel B of Figure 3), the X-ray flux above 3.5 keV flux exceeded the X-ray flux above 16 keV in the primary footpoint (pixel A) by factor 5 and the > 22 keV flux by factor > 30. Thus we confirm our conclusion from the preceding section that the X-ray emission at the secondary footpoint of the L arch could not be caused by electron streams. Nevertheless, electrons had to produce the initial Hα brightening. Even for that, as Equation (1) shows, one needs $E_m(0) > 37$ keV for $n_e = 10^{10}$ cm^{-3} and $E_m(0) > 12$ keV for $n_e = 10^9$ cm^{-3}. Thus the density in the L arch should be still lower than in the SB arch.

Let us remember (as mentioned in Section 4.2) that the presence of Hα emission indicates a density at least two orders of magnitude higher, in the excess of 5×10^{11} cm^{-3} (Zirin, 1987; Švestka *et al.*, 1987; Heinzel and Karlický, 1987). Thus it is of interest to inquire what density is found from the analysis of X-rays.

Unfortunately, the analysis of emission measure in the X-ray images yields only very rough estimates of the electron density, because of the low spatial resolution of HXIS; the resolution of ≈ 6000 km in the SB arch and 23 000 km in the L arch (as compared to < 1000 km in Hα) masks any fine structure; by introducing an unknown and arbitrary filling factor one can enhance the obtained density by one order of magnitude or more. Nevertheless, at least the minimum possible density (for filling factor $q = 1$) can be determined.

In the primary footpoint of the SB arch, at the time of its maximum brightness, a comparison of counts in the 3.5–5.5 and 5.5–8.0 keV energy bands yields temperature $T = 19.4 \times 10^6$ K and emission measure $Y = 4.8 \times 10^{48}$ cm^{-3} per one pixel of HXIS fine field of view (8 × 8 arc sec). Under the assumption of uniform n_e we find $n_e^2 = 2.23 \times 10^{31}/hq$, where h is the extension of the emitting region along the line-of-sight and q (≤ 1) is the filling factor. Table III gives the h values for various densities and different values of q. The same procedure was repeated for the central part of the arch ($T = 17.0 \times 10^6$ K and $Y = 5.5 \times 10^{47}$ cm^{-3}) and for the secondary footpoint ($T = 20.9 \times 10^6$ K and $Y = 4.8 \times 10^{47}$ cm^{-3}), also at the time of the maximum X-ray brightness at that site.

Table III shows that the n_e value in the X-ray emitting region near the primary footpoint would be close to 10^{11} cm^{-3} for a homogeneous arch structure, but could

TABLE III

Line-of-sight thickness of the SB arch (h, in km) for various densities n_e and filling factors q

n_e (cm^{-3})	$q = 1.0$	$q = 0.3$	$q = 0.1$	$q = 0.03$	$q = 0.01$
			Primary footpoint		
3×10^{10}	(158000)	( )	( )	( )	( )
10^{11}	14200	(47300)	(142000)	( )	( )
3×10^{11}	1520	5270	16000	(52700)	(160000)
10^{12}	(142)	(473)	1420	4730	14200
3×10^{12}	( )	( )	(158)	(530)	1580
			Top of the arch		
10^{10}	(163000)	( )	( )	( )	( )
3×10^{10}	18100	(60300)	(181000)	( )	( )
10^{11}	1630	5430	16300	(54300)	(163000)
3×10^{11}	(181)	(603)	1810	6030	18100
10^{12}	( )	( )	(158)	(530)	1580
			Secondary footpoint		
10^{10}	(142000)	( )	( )	( )	( )
3×10^{10}	15800	(52700)	(158000)	( )	( )
10^{11}	1420	4730	14200	(47300)	(142000)
3×10^{11}	(158)	(526)	1580	5260	15800
10^{12}	( )	( )	(140)	(470)	1400

The values in brackets are either too large (> 20000 km) or too small (< 1000 km).

grow to $\approx 10^{12}\,\mathrm{cm}^{-3}$ for a filamentary structure with $q \leq 0.1$. At the secondary footpoint the density results lower: $\approx 3 \times 10^{10}\,\mathrm{cm}^{-3}$ for a homogeneous structure and $\approx 3 \times 10^{11}\,\mathrm{cm}^{-3}$ for $q \leq 0.1$. Thus either the density or the filling factor was decreasing along the path from the primary toward the secondary footpoint. Since Figure 1 does not indicate any divergence of fieldlines near the secondary footpoint, a decrease in density along the arch is more likely. The emission measure for the arch top yields an intermediate density value, only slightly higher than the density at the secondary footpoint. However, the arch cross section might increase with the distance from each footpoint, with its maximum near the arch top. In the case of such a 'banana' shape it is to be expected that the average density at the top would be lower than for an arch with a constant cross section.

4.4. Hα AND X-RAY EMISSION WITHIN THE ARCH

We now consider the sequential appearance of X-ray and Hα emission in the arch. We will suppose that the leading edge of the moving X-ray feature has very high temperature and low density, with temperature decreasing and density increasing from the leading edge towards the tail of the injection. The leading edge is seen only in X-rays and the tail in Hα. It is not clear whether the tail has low temperature, needed for Hα emission, since its injection, or whether initially the whole plasma cloud is at coronal temperatures and the tail cools fast because of its high density. (This case will be discussed quantitatively in Paper II.)

The existence of neutral hydrogen since the onset of the injection must be considered possible, at least in the L arch, because the first visible sign of the arch was the observation of moving knots of Hα emitting mass. During the later phase of intense Hα emission, at those times when filtergrams have been taken in the wings of the Hα line, the filtergrams have always shown a Doppler shifted mass within the arch. Three important aspects of the evolution of the L arch are: (1) its beginning as rapidly moving, small knots of Hα emission followed by (2) a diffuse, fainter injection of Hα emission which (3) in turn evolved into a dense ejection of Hα-emitting mass. The maximum flux of X-ray emission within the arch corresponds to the phase when the fainter, diffuse Hα emission is seen. Thus, we cannot escape the possibility that at least some neutral hydrogen could be concurrently present during the X-ray phase of the L arch although this needs not necessarily be true for the SB arch. A simple way to account for the concurrent presence of Hα emission (neutral hydrogen) and X-rays is to infer that the arch is composed of many parallel threads of streaming plasma and particles and that the threads have widely differing temperatures. The analysis made in the preceding section indicates that these threads must also have widely different densities.

As the referee has pointed out, other possible ways to account for the concurrent presence of Hα and X-rays could involve the local production of electrons via ionization within the arch and the subsequent acceleration of the electrons by shock waves or by electric fields parallel to the magnetic field along the arch. Further analysis of these possibilities is beyond the scope of this paper.

4.5. Interpretations of Hα emission within the arches

During solar flares, the appearance of Hα emission at the chromosphere is considered to be thermal excitation. Recombination is stimulated by either heat conduction, fast streaming particles, or shock waves. The result is localized heating. However, in the case of flare loops, the appearance of emission at the tops of the loops has been successfully interpreted as the cooling of a hot coronal plasma. Thus, in the circumstance of flaring arches, we must ask whether the Hα components represent heating, cooling or the transfer of an injected, cool Hα emitting gas through the corona.

The early emission at the secondary footpoint is easily interpreted as heating of the chromosphere via Coulomb collision. The subsequent increase in footpoint emission can be further heating due to the influx of a greater number of particles, but in that case protons are needed as the exciter for the L arch. Thus this subsequent increase may be a consequence of another exciting agent, e.g., a conduction front as suggested by Rust, Simnett, and Smith (1985) (cf. Section 4.6).

The Hα emission within the arch can be viewed as (1) a similar collisional process, (2) cooling of plasma that originally was at coronal temperatures, or (3) the transfer of a cool, only partially inonized gas cloud from the source flare into the corona.

The third interpretation seems to be supported by the fact (mentioned in the preceding section) that at the onset of the L event Hα images showed discrete knots of emission traveling up the primary leg of the arch. Filtergrams taken during some flaring arch events confirm the Doppler shifts expected if the event is mass transfer through the arch. Thus we have substantial evidence that, at least in some arches (and in the L arch in particular), a significant fraction of the Hα emission was simply mass at chromospheric temperature entering the arch and propagating along it.

It is conceivable that some fraction of the Hα emission also appears due to cooling of the plasma previously seen in X-rays. In the SB arch the densities deduced from X-rays (Table III) confirm that this process should contribute to the observed emission in Hα, and the question is how important is this contribution, in particular in the smaller (and, hence, probably denser) arches of the SB type. We discuss this problem in Paper II, where observations of more arches of this kind will be presented.

4.6. Conduction front

The flares discussed here are two of the seven events listed by Rust, Simnett, and Smith (1985) in which they observed X-ray emission first at one end of a structure followed by the propagation of the X-ray emission along inferred magnetic field lines at a velocity between 800 and 1700 km s^{-1}. Our values of v(X-rays) in the SB arch and v_2(X-rays) in the L arch are within these limits. Values of v(X-rays) given by Rust *et al.* for these two events are 1040 km s^{-1} for the SB arch, in good agreement with our extimate, but 925 km s^{-1} in the L arch which is between our values of 480 km s^{-1} and 1640 km s^{-1} (cf. Section 3.3).

Rust, Simnett, and Smith have interpreted the gradual excitation of the loops as due to fast-moving thermal conduction fronts with steep temperature gradients, where fast

electrons have a mean free path much larger than the scale height of the gradient. While it is possible to assume that all the hot coronal mass is injected into the arch and the moving X-ray emission simply reflects its motion (as has been supposed in Section 4.4), the explanation proposed by Rust, Simnett, and Smith offers several advantages: (a) It can explain the X-ray emission at the secondary footpoint, without involving the highly hypothetical proton streams (though the harder X-ray spectrum at the secondary footpoint remains a problem). (b) It does not require a very high amount of material at extremely high coronal temperatures injected into the arch as the above explanation does. (c) In general, it fits the observed values of v(X-rays). And (d) it might help to explain the delay in the onset of the X-ray emission at the secondary footpoint mentioned in Section 3.9, if a shock develops in the arch in association with the front. It is quite likely that the hot material, ejected from the primary footpoint, gives rise to a conduction front and possibly also to a shock. Therefore, we will discuss this possibility again in Paper II, where we examine a model that combines the conduction front with radiative and conductive cooling of the heated plasma.

5. Summary

Flaring arches are a newly recognized high-energy component of some solar flares, detected in the corona in X-ray and Hα images. X-ray and Hα emission appear to flow into the corona from a primary footpoint in a flare with the X-ray component preceding the Hα flow. Both emissions follow the same arch-shaped trajectory to their final destination at a secondary footpoint which is located in the same active region at a distance of tens of thousands of kilometers. The secondary footpoint brightens in Hα within seconds after the onset of the flare-associated hard X-ray burst while the X-ray brightening at this footpoint is more delayed. But the maximum of brightness occurs at the secondary footpoint at the same time both in Hα and X-rays.

It is convenient to describe the flaring arch events as having three or four phases: (1) An early phase indicated by a brightening of the secondary footpoint in Hα which we deduce to be caused by the propagation of (low-density) energetic electrons through the arch. (2) A second phase characterized by X-ray emission propagating through the arch, accompanied by further brightening of the secondary footpoint both in Hα and X-rays. (3) A third phase characterized by the flow of Hα emitting mass through the arch but with no additional brightening of the secondary footpoint; and in some events (4) an aftermath when low-intensity Hα-emitting mass is seen to propagate in the reverse direction through the arch, sometimes associated with a new weak X-ray brightening.

The overall physical picture within the arches is that, at any given cross-section, there is an increase in density with time; the events start with low densities, of the order of 10^9 cm^{-3} during the early phase, increase to at least 10^{10} cm^{-3} during the X-ray phase and further increase to at least 5×10^{11} cm^{-2} during the Hα phase when the injected mass becomes visible in emission in the Hα line. The emission measure analysis during the X-ray phase reveals a density gradient within the arch, with density decreasing by an order of magnitude from the primary footpoint to the secondary one. One can

suppose that the density gradient is still steeper during the early phase and probably diminishes during the Hα phase.

The overall temperature structure of the arch is the inverse of the density structure: the early phase (corresponding to the early Hα brightening of the secondary footpoint) is clearly non-thermal; the X-ray phase corresponds to temperatures close to 20×10^6 K. During the late Hα phase the temperature drops to about 10^4 K.

From the speeds of propagation derived from the X-ray and Hα components (Sections 3.1 and 3.3), we see that the propagation of the various components through the arch follows the temperature pattern: the highest speeds are in the electron streams at the start of the event; intermediate speeds (sometimes different for different ejection components) are found for the X-ray phase (400–1900 km s^{-1}), and low speeds (less than 400 km s^{-1}) characterize the Hα phase.

The injection of mass into the flaring arches and the travelling X-ray emission along the arch are subjects that offer new challenges to the modelling of this component of some flares.

Acknowledgements

We are obliged to an unknown referee and Drs Giannina Poletto and Aert Schadee for constructive critical comments. The contribution of SFM to this paper was initiated under support from the Office of Naval Research under grant N00014–82–K–0733 and completed under grant N00014–82–K–0139. The development and construction of the HXIS was made possible by support from the Netherlands Ministry for Education and Science, and the Science and Engineering Research Council of the United Kingdom. Microwave radio data have been analyzed and kindly provided to us by Dr Gordon Hurford at Caltech. Mr Hans Braun at Utrecht skillfully prepared all the figures.

References

Brown, J. C.: 1971, *Solar Phys.* **18**, 489.
Bruzek, A.: 1967, *Solar Phys.* **2**, 451.
Dennis, B. R., Orwig, L. E., Kiplinger, A. L., Gibson, B. R., Kennard, G. S., and Tolbert, A. K.: 1985, *The Hard X-Ray Bursts Spectrometer Event Listing 1980–1985*, NASA TM 86236.
Duijveman, A., Hoyng, P., and Machado, M. E.: 1982, *Solar Phys.* **81**, 137.
Heinzel, P. and Karlický, M.: 1987, *Solar Phys.* **110**, 343.
Hoyng, P., Brown, J. C., and van Beek, H. F.: 1976, *Solar Phys.* **48**, 197.
MacNeice, P., Pallavicini, R., Mason, H. E., Simnett, G. M., Antonucci, E., Shine, R. A., Rust, D. M., Jordan, C., and Dennis, B. R.: 1985, *Solar Phys.* **99**, 167.
Martin, S. F.: 1979, *Proc. US-Indo Workshop on Solar Terrestrial Physics*, 12–16 June 1979, Udaipur, India, p. 25.
Martin, S. F. and Švestka, Z.: 1987, *Bull. Am. Astron. Soc.* **18**, 898.
Mewe, R., Gronenschild, E. H. B. M., and van de Oord, G. H. J.: 1985, *Astron. Astrophys. Suppl.* **62**, 197.
Mouradian, Z., Martres, M. J., and Soru-Escaut, I.: 1983, *Solar Phys.* **87**, 309.
Orwig, L. E., Frost, K. J., and Dennis, B. R.: 1980, *Solar Phys.* **65**, 25.
Rust, D. M. and Webb, D. F.: 1977, *Solar Phys.* **54**, 403.
Rust, D. M., Simnett, G. M., and Smith, D. F.: 1985, *Astrophys. J.* **288**, 401.
Solar Geophysical Data: 1981a, No. 437, Part I, p. 126.

Solar Geophysical Data: 1981b, No. 441, Part II, p. 26.
Solar Geophysical Data: 1983, No. 467, Part 2, pp. 34 and 49.
Švestka, Z.: 1984, *Solar Phys.* **94**, 171.
Švestka, Z.: 1987, *Solar Phys. (Letter)* **108**, 411.
Švestka, Z., Schrijver, J., Somov, B., Dennis, B. R., Woodgate, B. E., Fuerst, F., Hirth, W., Klein, L., and Raoult, A.: 1983, *Solar Phys.* **85**, 313.
Švestka, Z., Fontenla, J. M., Machado, M. E., Martin, S. F., Neidig, D. F., and Poletto, G.: 1987, *Solar Phys.* **108**, 237.
Švestka, Z., Fárník, F., Fontenla, J. M., and Martin, S. F.: 1988, *Solar Phys.* (in preparation, Paper II).
Tang, F.: 1982, *Solar Phys.* **77**, 263.
Van Beek, H. F., Hoyng, P., Lafleur, B., and Simnett, G. M.: 1980, *Solar Phys.* **65**, 39.
Zirin, H.: 1987, *Astrophysics of the Sun*, Cambridge Univ. Press, Cambridge.